Arch. Metall. Mater. **69** (2024), 2, 639-651

DOI: https://doi.org/10.24425/amm.2024.149793

M. HIDIROĞLU[1], T.A. BAŞER[1], N. KAHRAMAN[2]

MICROSTRUCTURE AND MECHANICAL PROPERTIES OF DISSIMILAR RESISTANCE SPOT WELDED ZN-COATED DP800–TBF1180 AUTOMOTIVE STEELS USING MFDC TECHNOLOGY

The use of advanced high-strength steel in the automotive industry is increasing in last decade. This is due to the restrictions to reduce fuel consumption and thereby decrease harmful carbon dioxide emissions. This paper aims to investigate welding properties of dissimilar resistance spot welded hot dip galvanized DP800–TBF1180 automotive steels using MFDC (Mid Frequency Direct Current) technology. LME crack occurrence due to the zinc coating was determined by magnetic particle test. The mechanical properties of welded joints were determined by tensile-shear, cross-tension and hardness measurements. The micro structural characterization was also performed in the weld zones of the joints. The appropriate welding parameter range were selected for welding processes by MFDC technology. Therefore, LME crack formation were not observed according to magnetic particle test. The highest strength was obtained as 17.60 kN and 5.51 kN by tensile-shear and cross tension tests, respectively with a welding current of 8 kA. In addition, a soft zone was found in the HAZ for both base metals. The hardness decrease in HAZ is more pronounced on the TBF1180 side. The soft zone hardness values of the sample S4 were approximately 330 HV, and the hardness values of the base material were measured in the range of 376-386 HV.

Keywords: DP800 steel; TBF 1180 steel; MFDC; resistance spot welding; welding current; liquid metal embrittlement

1. Introduction

The weight reduction in the automobile industry through the use of advanced high strength steels (AHSS) became important in the automobile industry. AHSS provide thinner vehicle component production to achieve light weighting. AHSS are also crucial for the crash performance of automobile structural safety components as A and B pillar, roof header, roof rail, door impact beam, seat and tunnel reinforcements [1]. However, problems can occur after stamping and welding operations of these steels with over 1000 MPa in tensile strength [2,3]. Zn coating (Galvanized coating) is generally used in AHSS steels to prevent corrosion [4,5]. Resistance spot welding (RSW) is generally preferred joining method for vehicle body assembly process due to its low cost, ease to operation and rapid welding advantages. However the Zn coated AHSS are rather susceptible for liquid metal embrittlement (LME) cracking during RSW [4]. LME crack formation can deteriorate the spot weld ability of Zn-coated AHSS during RSW [6,7]. The zinc element in the galvanize coating starts to melt 420°C and then liquid zinc occurs on the sheet surface during RSW. The molten zinc penetrates into the steel matrix which causes LME cracks [8,9]. The mechanical performances of the spot welds can be affected by LME cracks. The Zn-coated advance high strength steels exhibit cracks of liquid metal embrittlement (LME) due to increase of tensile stress from heating, cooling, and melting of Zn during resistance spot welding or hot stamping process [10].

Hence, these cracks need to be eliminated. RSW is a type of fusion welding process in order to obtain welded parts in automobile production lines. During RSW, required heat for melting is generated by passing a high current through small spots using copper electrodes [11]. Mid-frequency direct current (MFDC) technology can bring benefits and advantages compared to conventional alternative current (AC) technology [12]. In recent years, MFDC technology with 1000 Hz medium frequency current tends to replace 50 Hz resistance welding machines (single phase AC). A considerable amount of reduction in the size and weight of the transformer is achieved by MFDC technology. Within this technology, the electrodes are mounted on the end of the robot arm by creating a short path for the welding current. In addition, DC welding current provides much greater control and welding consistency respect to AC current [13].

[1] COŞKUNÖZ MOLD MACHINE, R&D CENTER, BURSA, TURKEY
[2] KARABÜK UNIVERSITY, DEPARTMENT OF MANUFACTURING ENGINEERING, KARABÜK, TURKEY
* Corresponding author: mhidiroglu@coskunoz.com.tr

For the MFDC technology, welding can be done 30 times faster than the AC technology. MFDC technology can prevent most of the thermal deformation and spatter which might occur during RSW with AC technology by rapid welding. LME crack propagation can be avoided by MFDC features due to reduced welding time [11-13].

In this study, a pre-pulse low current was applied in order to reduce the main welding pulse time with a lower heat input. Ashiri et al. found that LME cracks might initiate when the critical nugget diameter is reached. It was also stated that LME cracks occur during the second welding pulse [8,14]. In this case, it can be said that parameter design with multi-pulses contributes to LME crack propagation.

Researchers emphasized that excessive heat input should be avoided to control LME sensitivity. (eg. excessive welding time and current) [15]. Applying a pre-pulse that generates enough heat to melt the coating causes an increase in LME intensity due to increased heat input. These observations contradict with the previous literature. According to the World Auto Steel report, pre-pulsing cannot evacuate the zinc from the welding area before the main welding process [16]. However, low current (4 kA) pre-pulses stabilize the zinc via iron diffusion without melting the coating, thereby reducing LME cracking [17].

Yılmaz et al. investigated the correlation between crack depth and the heat input. It was found that the crack depth increased with the increase in heat input [18]. Therefore, LME cracking can be avoided to reduce heat input as well as the welding current and welding time. Increasing the electrode force can also reduce the heat input by reducing the contact resistance between the welded plates [19,20].

In this study, in order to contribute to the mechanical and performance expectations of the automotive industry, hot-dip galvanized DP800 and TBF1180 high-strength steels with different thicknesses were joined by RSW method. A test matrix was constructed by using low pre-pulse current. In addition, the main pulse current was gradually increased. LME crack formation was primarily investigated. The effect of the main welding pulse current on the microstructure, hardness and mechanical properties of the welded joint were evaluated by tensile-shear and cross-tension tests. Pre-pulse temperature values on the TBF 1180 surface were determined by simufact welding software. Thus, while the test matrix was being prepared, it was aimed not to reach the melting point of the galvanized coating on the welding surface of the TBF1180 material.

2. Experimental procedures

In this study, GI coated DP 800 and TBF 1180 steels were used. The nominal sheet thicknesses of DP800 and TBF 1180 steels are 1.2 mm and 1.5 mm, respectively. The TBF steel and DP800 steel respectively with a yield strength of 774 (±4.7) MPa and 456 (±4.3) MPa, tensile strength of 1104 (±3,63 MPa and 757 (±3,72), elongation of 16.7 (±0.5) % and 16.3 (±0.5) % was used. Elemental analyses of sheet materials were carried out with the GNR Atlantis brand Optical Emission Spectrometer device. The weight % chemical compositions of base materials were shown in TABLE 1.

The DP800 and TBF 1180 steel plates were prepared by laser cutting in 30×100 mm dimension. The surface of the steel plates was cleaned by ethanol in order to remove the oil, dirt and scales before RSW. The RSW was performed when the steel plates overlapped as 30 mm. Serra Soldadura mark MFDC RSW technology was used. The electrode cap tip is type G with a 6 mm diameter and the electrode material is chrome-zirconium-copper alloy. RSW parameters by MFDC are shown in TABLE 2. In order to break coating layer and to reduce the duration of the main welding pulse pre-pulse stage was added (TABLE 2). Afterwards, the weld nugget was produced using main pulse current (TABLE 2).

According to preliminary studies, the optimum spot diameter was calculated using the formula, $d_p = 5.5\sqrt{t}$, where d_p is the

TABLE 1

The chemical composition of DP 800 and TBF 1180 base material (wt. %)

Material	C	Si	Mn	P	S	Al	Nb+Ti	Cr	Cu	Ni+Cu	Cr+Mo	B	Fe
TBF1180	0.23	2.0	2.9	0.040	0.010	0.020	0.15	—	0.20	—	0.6	0.005	Rest
DP 800	0.15	0.20	1.72	0.012	0.003	0.040	0.20	0.42	—	0.050	—	—	Rest

TABLE 2

Welding parameters used in the study

Spec. no	Pre-Pulse			Main Welding Pulse				HII*
	Current [kA]	Electrode Force [daN]	Welding time [ms]	Current [kA]	Electrode Force [daN]	Welding time [ms]	Number of pulses	
S1	3	500	150	7	500	500	1	25850
S2	3	500	150	7,5	500	500	1	29575
S3	3	500	150	8	500	500	1	33350
S4	3	500	150	8.5	500	500	1	37475
S5	3.5	500	150	7	500	500	1	26338
S6	3.5	500	150	7.5	500	500	1	29963

* In the calculation of the HII, the units of weld current and welding time were described as “kA” and “ms”, respectively.

optimum spot diameter and t is the material thickness. Minimum spot diameter (d_{pmin}) should be as $4\sqrt{t}$. The heat Input index (HII) for each welded joints were calculated according to formula of $Q = KI^2Rt$, where Q is the heat generated, K is the heat losses, I is the welding current, R is the resistance across the electrodes, t is the welding time. R and K were considered constant (=1) in the heat input equation because all spot-welds were produced at constant electrode force and under the same welding conditions.

Parameters were determined using the operator experience, and Magnetic particle Inspection (MPI) and macrostructure investigations were used while determining the parameters.

A tensile-shear and cross-tension draw fixture were manufactured for the RSW welding following to the related standards. The both shear tensile and cross-tensile tests were produced according to EN ISO14273 standard. The welding operations were carried out through these fixtures. The molds for welding processes and tensile test set up are shown in Fig. 1.

LME cracks were determined by magnetic particle tests before metallographic specimen preparation. DP800-TBF 1180 welded joints were cut out from the nugget centre by METKON METACUT 302 metallographic sensitive cutting equipment. Cross section of welded specimens was mold by METKON ECOPRESS 52 hot molding machine. The standard metallographic grinding and polishing were performed by METKON FORCIPOL 202 unit. Welded joints were etched by 2% Nital solution for the macro/micro structural investigations. Cross section of DP800-TBF 1180 welded joints were examined by Nikon SMZ745T optical microscope. Dimensions of tensile shear and cross tension tests are illustrated in Fig. 2. Specimens in 100×30×1.2 mm and 100×30×1.5 dimensions were prepared according to EN ISO 14273 standard for both shear tensile and cross tensile tests.

Tensile-shear and cross-tension tests were performed at 50 kN capacity SHIMADZU equipment rate at room temperature with 5 mm/min tensile speed. Fig. 2 shows the geometry of the tensile-shear and cross-tension test specimens as well as the test set-up. Three specimens were used for each welding parameter in order to see the repeatability of the test results.

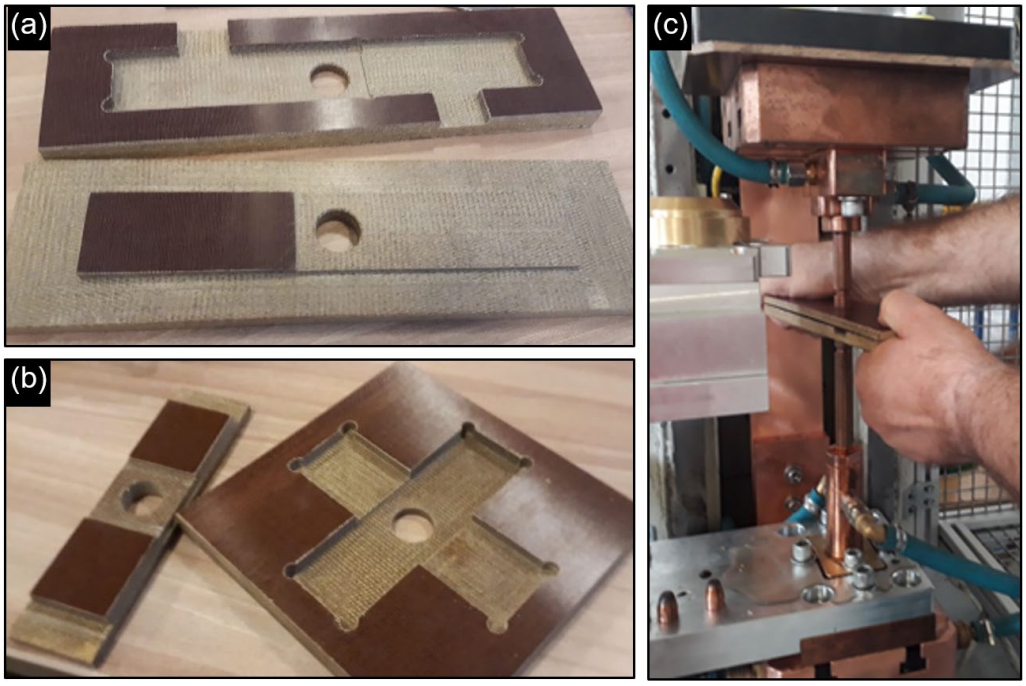

Fig. 1. Illustration of welded joints; (a) tensile shear test and (b) cross tensile test specimen preparation, (c) tensile test set up

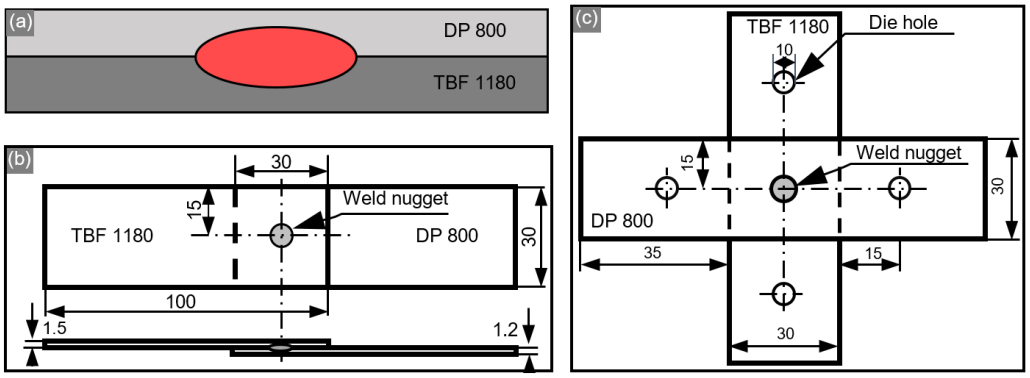

Fig. 2. Illustration of; (a) weld nugget position, (b) tensile-shear and (c) cross-tensile test specimens (EN ISO 14273)

Shimadzu HMV-2 micro hardness tester was used with 500 g load and a dwell time of 15 seconds to see the Vickers method HV0.5 hardness values variation in base materials, weld metal and heat effected zone (HAZ). The verification of the simulation results against experimental results is always a prerequisite to ensure that the results are valid. But In order to consider the temperature values occurring on the spot surface welded by the pre-welding puls a commercial FEA solver Simufact Welding® has been employed and for 3kA pre-puls have been simulated.

3. Results and discussions

3.1. Magnetic particle test results

The magnetic particle test results of nugget front and back surfaces are shown in Fig. 3. According to magnetic particle test images, LME cracks were not observed on the weld nugget and it's around (Fig. 3).

LME cracks were not observed on the weld surface according to magnetic test results. LME cracks in the weld core and surrounding HAZ adversely affect the mechanical properties and corrosion resistance of welded joints. During RSW, the liquid zinc is absorbed by the material. This causes a decrease in adhesion strength and crack formation along to the grain boundaries. Within the study, there are two challenges in order to avoid LME crack formation; i) welding processes have been carried out in DC current instead of AC by MFDC RSW technology, ii) welding parameter range were selected appropriately. LME crack formation was not allowed by MFDC technology with a shortened welding time and lower heat input.

Some researchers, [4,18,21-23] have stated that the electro galvanized zinc coating on the sheet surface and excessive welding heat input have a strong effect on the LME and surface-initiating cracks. Ashiri et al. [8] compared the LME crack sensitivities of galvanized (GI), Galva-annealed (GA), and electro galvanized (EG) Zn coatings. They reported that the LME crack sensitivity was lowest for EG coated steel plates due to the formation of α-Fe (Zn) layer from alloying of the coated layer during high-temperature processes and resistance spot welding. According to Ling et al. [24], the changes in LME crack sensitivity depending on the variables related to resistance spot welding (welding current, time, and electrode force etc.) were reported. Welding current and welding time cause heat input increase. The sensitivity of LME increases with the increase in heat input. It was observed that the depth of the LME cracks formed increased as the welding time increased. The increase in the electrode strength facilitates the advancement of the liquid zinc between the grains and increases the LME formation.

3.2. Macro/microstructure investigations

Macro/microstructure investigation was performed on the weld zone of the welded joints. Due to the large number of welding parameters, only the S3 (the most suitable parameter in the study) and S5 welded joints were shown in detail as an example. Figs. 4 and 5 show the macro/microstructural investigation of S3 and S5 welded joints, respectively. Three different zones were observed as the melting zone (weld nugget), HAZ and the base material according to macro structure images in Figs. 4 and 5. It was also observed that the grains elongated and banding along to the rolling direction of DP 800 and TBF 1180 base material. Considering that HAZ is a part of the base material and exposed to high temperature without melting, it was seen that banding disappeared in this region due to the effect of temperature. The cracks, porosity, voids or incomplete gaps were not observed in either of the weld metal (weld nugget) and HAZ.

The melting border was clearly observed on the DP 800 region in both macro structures. Whereas, this border cannot be distinguished on the TBF 1180 region. It can be said that the nugget may not have been obtained symmetrically in the cross-section of both materials due to the different chemical composition and electrical resistivity. In addition, different material thicknesses may be effective in the formation of non-symmetrical nugget.

Aydın et al. [25] studied on welding of DP 600 and TBF 1180 materials by RSW at different welding currents and the macro/microstructures of the welded joints were examined. It has been stated that there is a melting zone where the two

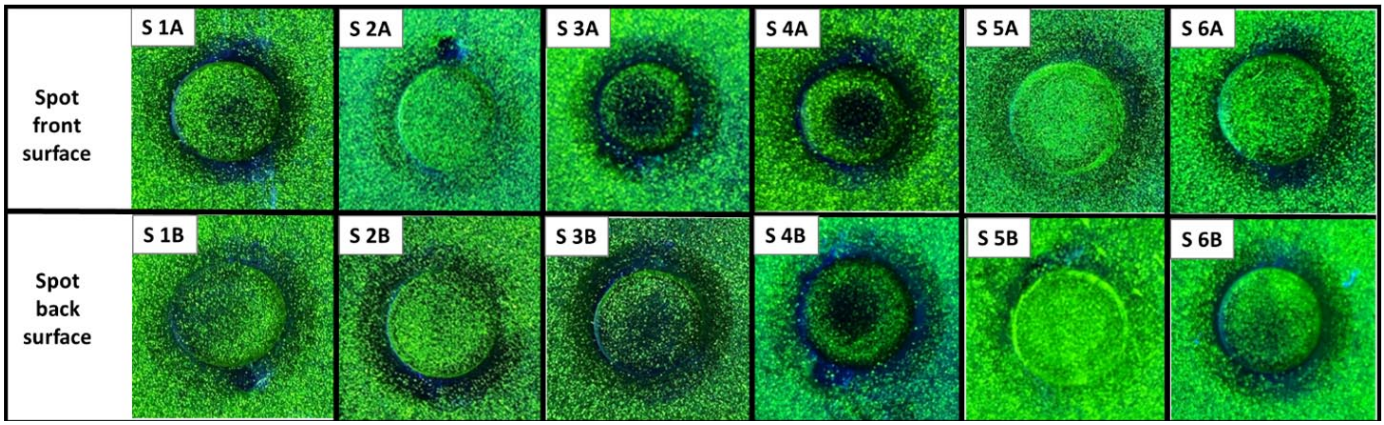

Fig. 3. Magnetic particle test results on weld nugget surface

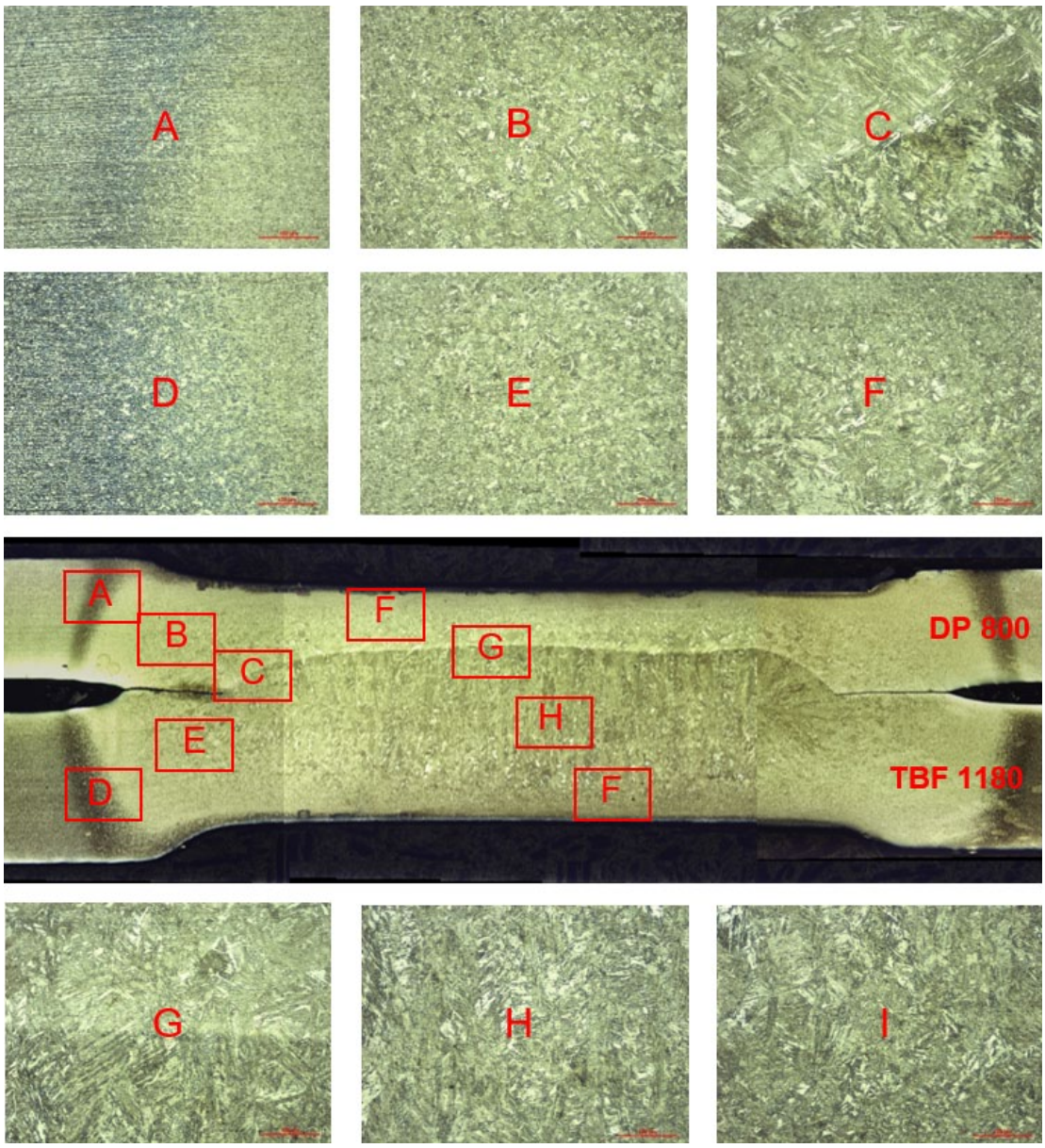

Fig. 4. Micro structural investigation on the intersection of the S3 welded joints

metals mixed and a partial melting zone where the mixing did not occur completely on the DP600 region. The reason for the formation of partial melting was explained as the rapid cooling conditions in the weld area and the lack of sufficient diffusion time. In addition, it has been reported that the differences in chemical composition, electrical resistivity and microstructure might be the cause of partial melting occurrence.

The above-mentioned three regions were divided into i) coarse-grained heat affected zone, ii) fine-grained heat-affected zone and iii) temperate zones in Figs. 4 and 5. In Fig. 5, parts A, B and C represent the temperate zone, fine-grained zone and coarse-grained zone in DP 800 material, respectively. Similarly, on the TBF 1180; the G, H and I sections represent the coarse grained, fine grained and temperate regions, respectively.

According to aforementioned observations, the part that completely turned into austenite due to the high temperature in welded joints during welding has a coarse-grained structure. However, it was determined that the finer-grained structure occurred on the part exposed to relatively lower temperatures.

The coarse-grained HAZ of the welded joints, which turned into fully austenite, generally transformed into bainitic and martensitic structures depending on the cooling rate after welding.

This region obtained rather hard and brittle due to the occurred phases. High temperature and austenitization caused coarse austenite grains. After cooling, the final microstructure became relatively coarse-grained.

The upper critical heat-affected zone (UCHAZ) consists of the UCHAZI, also called coarse grain zone, and the UCHAZII, also called fine grain zone. In the UCHAZ, the material is heated over the A3 temperature and therefore fully austenitized. Consequently, the microstructure is martensitic after quenching. The temperature in the intercritical heat-affected zone (ICHAZ) rises to a level between A1 and A3, and its microstructure after quenching consists of ferrite and martensite. The peak tempera-

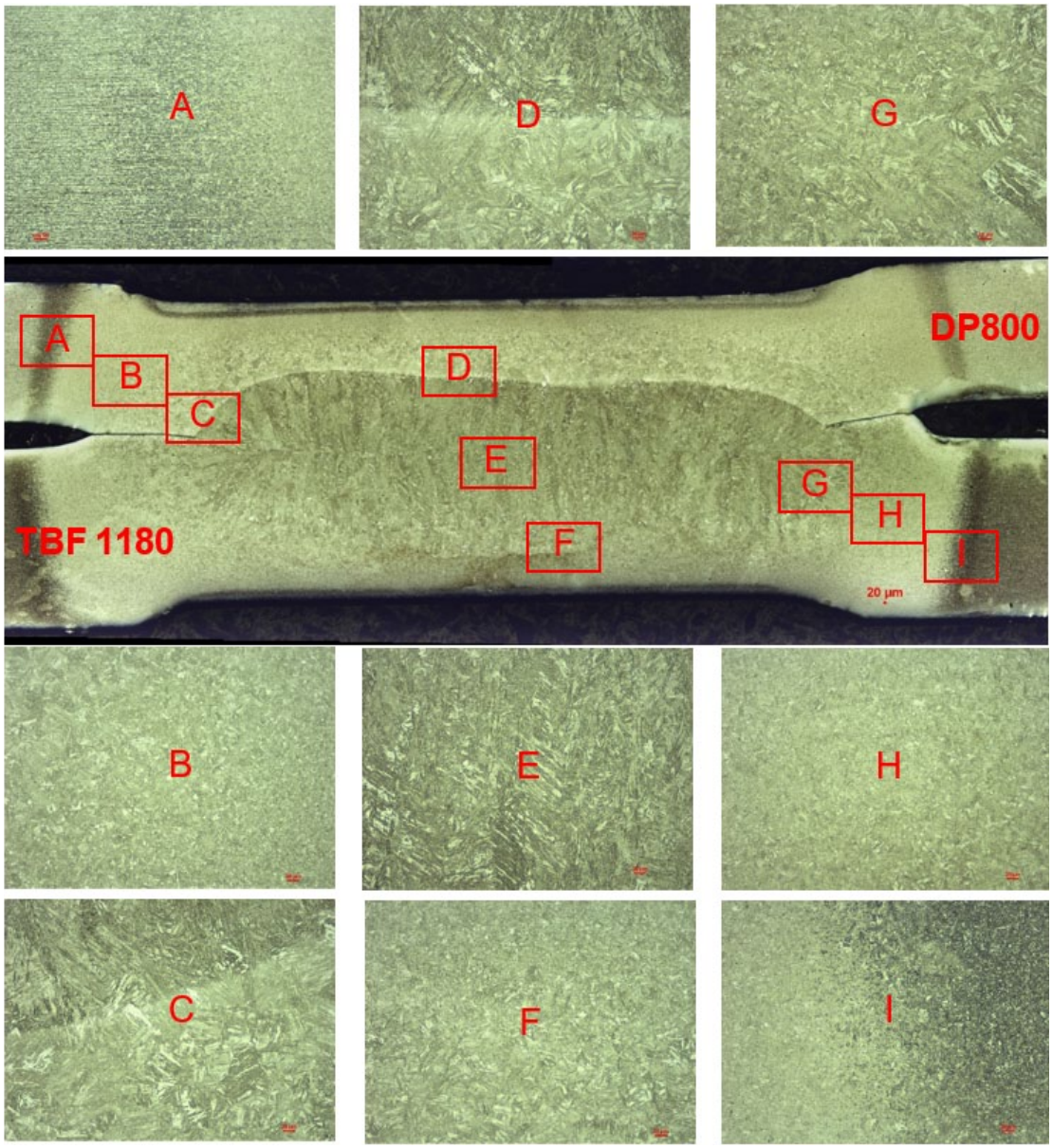

Fig. 5. Micro structural investigation on the intersection of the S5 welded joints

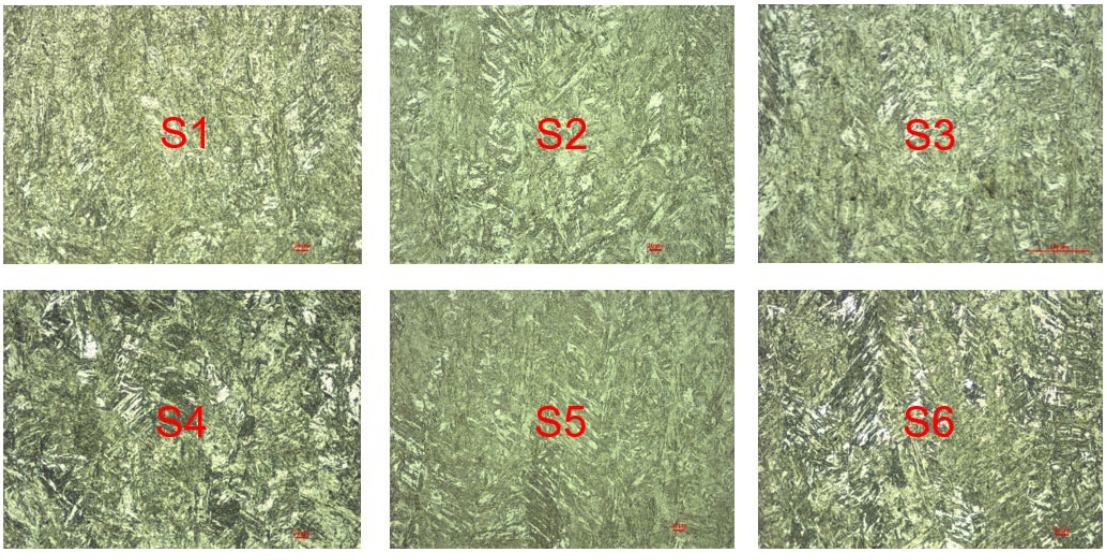

Fig. 6. Microstructures of weld metals a) S1, b) S2, c) S3, d) S4, e) S5 and f) S6

ture in the subcritical heat- affected zone (SCHAZ) is lower than the A1 temperature. Tempering of the microstructure occurs in this area and leads to softening [26]. The HAZ region where softening occurs is the border of the base material (SCHAZ) and its hardness value is lower than the base material. Therefore, failure defects can occur at the interface of the welded joint.

In Fig. 6, similar weld metal microstructures were observed. It was seen that the weld metal microstructures are quite different from the base material and HAZ microstructures. The grain sizes of weld metal was observed larger than base material and HAZs. The cooling rate can be changed depending on the heat input during welding. It is known that high heat input effective in grain growth.

In addition to the optical microscope studies, SEM (Scanning electron microscopy) and EDS (Energy dispersive spectroscopy) studies were also performed only for the sample S3 with the highest tensile shear load.

The microstructure images obtained in the nugget regions of the welded samples given in Fig. 7 are evaluated, a martensite structure is formed in the nugget zone during RSW due to heating and sudden cooling at high speeds. In other words, in Fig. 7, this crooked martensite structure with super saturated carbon is also seen in the SEM images.

As a result of BSD-EDS analysis results on S3 sample (Fig. 8), it is seen that the carbon ratio % in the white regions (number 1 coded region) is less than the carbon ratio % in the black region (number 2 coded region). In region 3, where a wide area was scanned, a value was obtained close to the average of regions 1 and 2. Banadkouki and Fereiduni [27] investigated different martensite region formation. Their SEM/EDS analysis on DP steels showed that different martensite regions were formed depending on different carbon ratios %.

3.3. Tensile-shear test

The tensile-shear graphs obtained from the average values are given in Fig. 9. In addition, the relationship between the HII index and the tensile strength is given in the graph in Fig. 10.

The highest tensile-shear load was obtained as 17.60 kN on S3 welded joint with a 8 kA welding current. As welding current increased to 8.5 kA, the tensile-shear strength decreased to 12.84 kN due to the expulsion on the intersection of S4 welded joint. The pre-pulse current was increased to 3.5 kA during the welding of S5 and S6 welded joints. It was observed that, tensile-shear strength of S1 and S2 (at 3 kA pre-pulse current) obtained

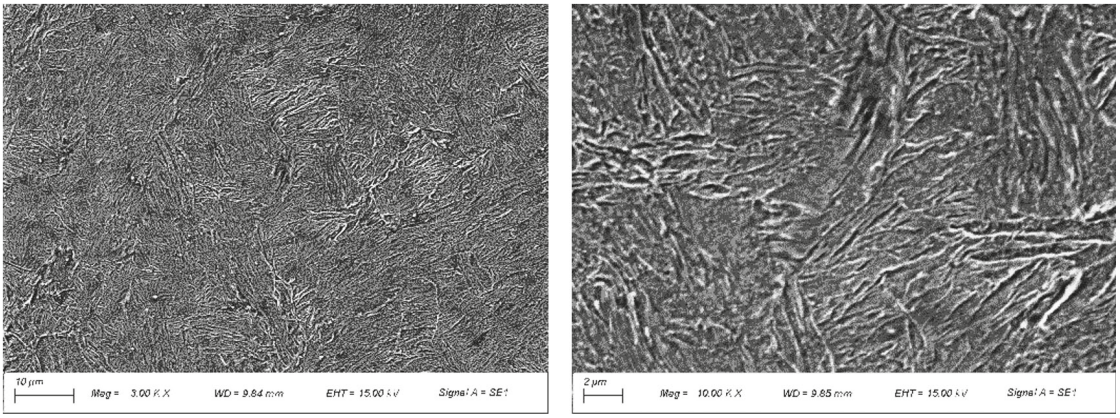

Fig. 7. SEM images of the nugget of the S3 sample at different magnifications

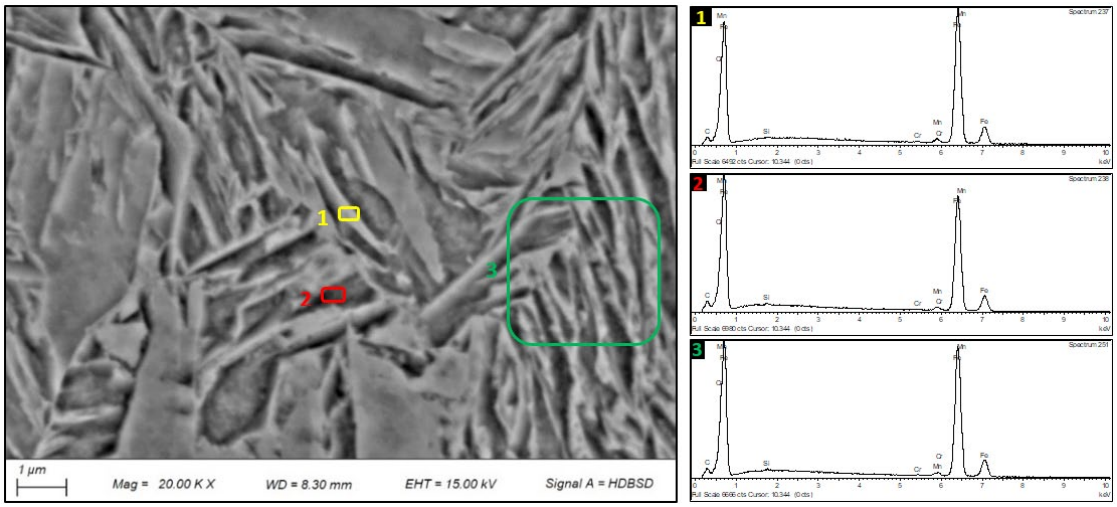

Fig. 8. BSD-EDS analysis results of S3 sample with a 20 kX magnification

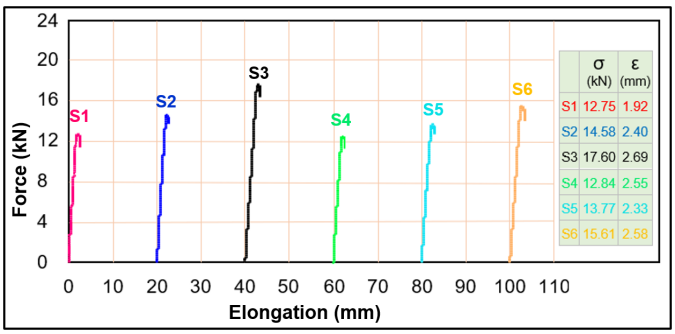

Fig. 9. Tensile-shear curves of joints

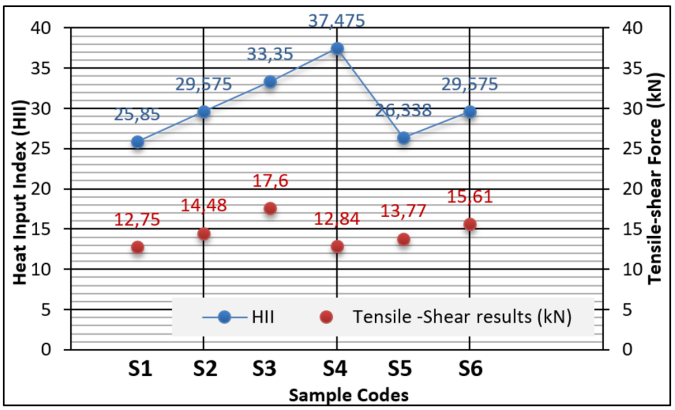

Fig. 10. The relationship between the HII index and the tensile strength

lower than the tensile-shear strength of S5 and S6 (at 3,5 kA pre-pulse current). It was concluded that pre-pulse current increased the tensile-shear strength of the welded joints by approximately 7-8%. In other words, it was determined that the tensile-shear strength increase up to a certain point depending on the increase in the main welding current, but the strength decreases due to the expulsion at the interface of welded joints.

The relationship between the heat input index (HII) and shear tensile test results is clear. As the HII index increased, the shear tensile test result values increased. However, since expulsion occurred in the sample S4, shear tensile value decreased. The relationship between the tensile test results of the samples S1 and S2 and the HII index was evaluated, increasing the main welding pulse from 7 kA to 7.5 kA increased the HII index and tensile strength. The increase in tensile strength between samples S1 and S2 is approximately 13%. The relationship between the tensile test result values of the samples S1 and S5 and the HII index was evaluated, the 0.5 kA value increase in the pre-heating welding pulse increased the HII index value and the joint strength by 7.8%. In the relationship between the tensile test and HII index of the samples S2 and S3, it was observed that the connection strength increased by 21% as a result of increasing the main welding pulse current value from 7.5 kA to 8 kA. In the relationship between the tensile test and HII index of the samples S2 and S6, it was determined that an increase of 0.5 kA in the pre-heating pulse increased the joint strength by 6% and the HII value.

It ensures that the electrode indentation depth in the welded specimens does not exceed 30% of the thickness of the welded material. In this case, the mechanical properties deteriorate [28].

Within the study, the electrode indentation depth did not exceed this recommended standard value of 30%.

In RSW, the increase in welding current increases the nugget diameter. Thus the strength is increased. The nugget sizes-mechanical property relationship is given in Fig. 11 where a: electrode indentation depth-nugget diameter, b: nugget diameter-tensile-shear/cross-tension results.

As the welding current increases, the nugget size as well as the maximum force ability also increase in RSW joints. Kaya and Kahraman [29], Fukumoto et al. [30], Sun et al. [31], Marashi et al. [32] investigated RSW of different materials and stated that increasing the welding current increases the tension-shear load carrying capacity.

Fig. 12 shows the fracture modes of the S1 (a), S3 (b), S4 (c) and S5 (d) welded joints after the tensile-shear test. Fracture mode is one of the validation parameters on welding quality in automotive industry. Nugget pull out fracture is preferred after tensile shear test. Nugget pull out fracture describes the reliability of the welding parameters. Nugget diameter and strength increased with increasing of heat input [33].

Interfacial fracture mode occurred on the S1 welded joint. Whereas, fracture occurred in nugget pull out fracture on S2, S3, S4, S5 ve S6 welded joints. In Fig. 12, it is worth to mention that the sizes of nugget pull out fractures were observed different in all welded joints. For instance, while the smallest nugget size was obtained in the S2, the largest nugget size was shown in S3. The size of nugget pulls out fracture depends on the tensile-shear strength of the welded joints. The S2 welded

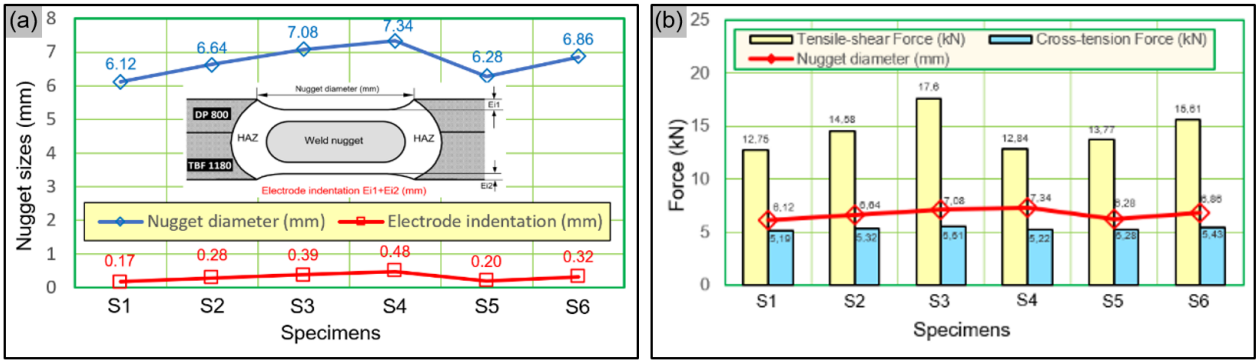

Fig. 11. The nugget sizes-mechanical property relationship

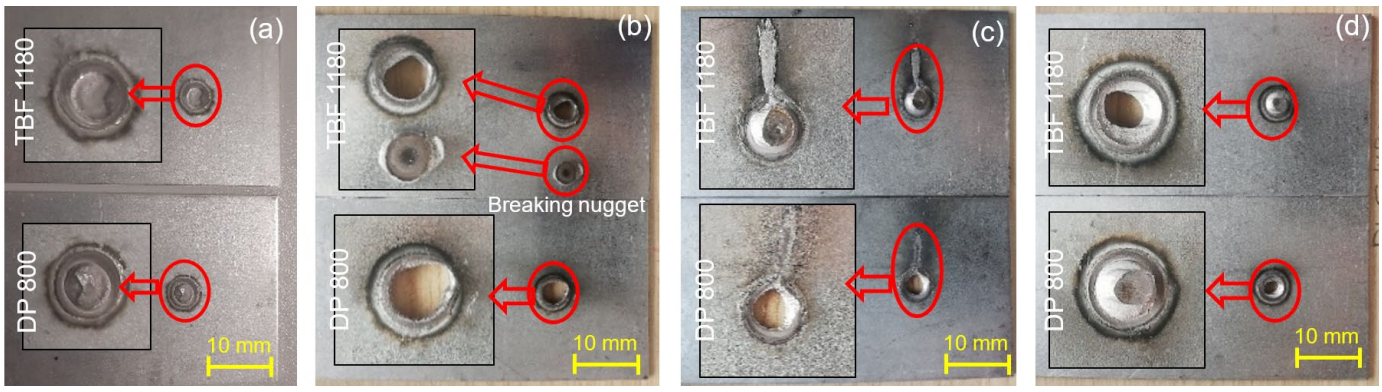

Fig. 12. The fracture modes of the S1 (a), S3 (b), S4 (c) and S5 (d) welded joints after the tensile-shear test

joint with nugget pull out fracture mode exhibited the lowest strength, while the S3 welded joint with nugget pull out fracture mode showed the highest strength.

Interfacial expulsion occurred in S4 welded joint due to the higher heat input value (TABLE 1).

The size of weld nugget increased depending on the increase in the heat input during welding. Therefore, the strength properties are improved. However, after a certain value, the strength properties were deteriorated by the expulsion at the interface. The nugget size, which grows with increasing heat input due to increasing welding parameters, decreases again with excessive melting and expulsion above a certain value (Fig. 12-S4).

Fig. 13 shows the welding capability diagram using for the evaluation of welded joints by RSW. This diagram is divided into four regions. According to Fig. 13; there is no melting or coalescence in region A. weaker weld joint occurs without melting in the B region that is formed by the welding pressure. Zone C corresponds to the melting or weld zone. Melting starts from the boundary curve of the C and B regions and the ratio of the molten weld region increase as it is included in these region. In practice, welding current and time values are chosen close to the upper limit of the C region. Region D is the expulsion region that starts from the upper border of region C. The interfacial failure mode occurred in B region (B: wet joining) on the S1 welded joint. When all parameters were kept constant and the welding current was increased from 7 kA to 7.5 and 8 kA, the failure mode converted from interface to nugget pull out. This zone is indicated by C (C: weld zone) on the diagram in Fig. 13. In this region, the electrode indentation depth was chosen not to exceed 30% of the base metal thickness. S2, S3, S5 and S6 welded joints were positioned in the C region in the weld ability diagram to provide appropriate mechanical properties. Within the study, only the S4 welded joint took its place in the D region (D: Expulsion zone) due to its high welding current values. In this region, high welding current values caused expulsion and thus a slight decrease in mechanical properties was observed.

It has been reported that the nugget size, which grows with increasing heat input due to increasing welding parameters, starts to decrease with excessive melting and expulsion above a certain value [30,32]. The weldability windows of the steels were developed to determine process robustness and acceptable welding zones for different welding times [32]. In this study, acceptable welding zones were determined according to different welding current values and marked on the welding loop graph seen in Fig. 13.

Spena et al. [34] studied the welding of Q&P and TRIP steels by RSW at different parameters. In general, they reported that in general nugget pull out fracture mode was observed. Due to the high welding current and expulsion, limited mechanical properties was obtained.

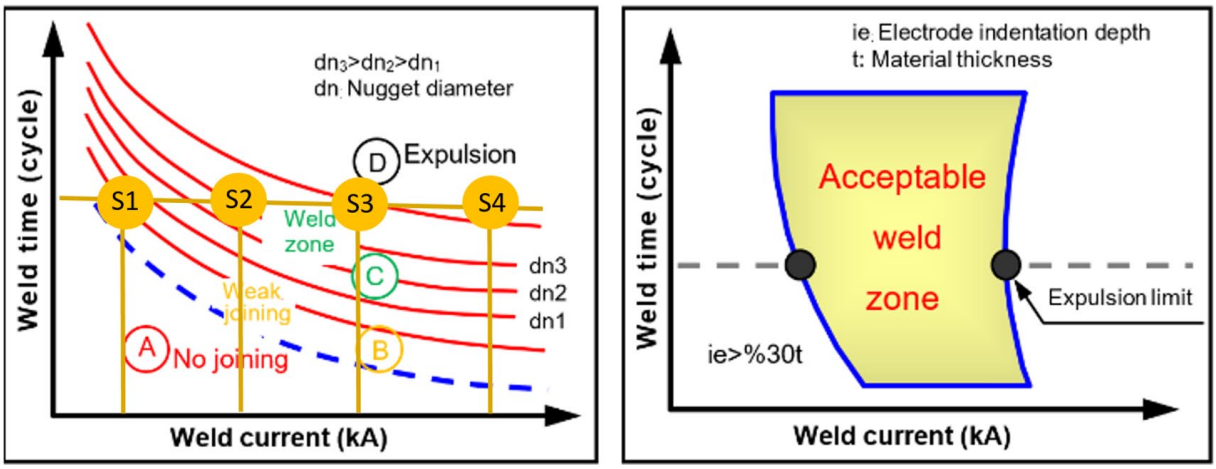

Fig. 13. Weld lobe curve. The location of the samples (S1, S2, S3 and S4) in the weld curve is marked

3.4. Cross-tension test

The cross-tension graphs obtained from the average values are given in Fig. 14. The highest cross-tension load was obtained as 5.51 kN on S3 welded joint with a 8 kA welding current. As welding current increased to 8.5 kA, the cross-tension strength decreased to 5.22 kN due to the expulsion on the intersection of S4 welded joint. For the S1 and S5 welded joints the same main welding current was used. As pre-pulse welding current increased (TABLE 1), a slight increase in cross-tensile strength was observed.

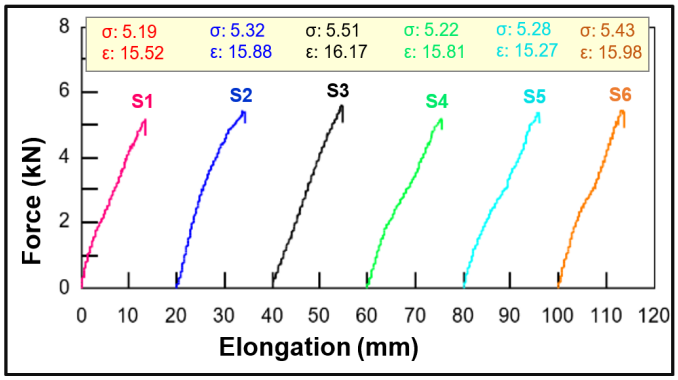

Fig. 14. The cross-tension tests results of welded joints

The cross-tension load carrying capacity depends to weld nugget size. As the welding current increases, the nugget size increased till expulsion starts, thus the weld strength increased proportionally as the load carrying region around the melting zone increased. The accuracy of the optimum welding parameter determined by the tensile-shear test was also confirmed by the cross-tension test results. The welding current is one of the important parameter for the occurrence of heat input on the weld interface by RSW.

According to heat formula $Q = K.\ I^2.R.t$, where, Q, I, R, t and K are generated heat input, welding current, electrical resistance, welding time and heat losses, respectively. The heat is directly proportional to the square of the welding current. The heat input increases with increasing welding current, since the rest of the parameters being constant. The increase in heat input causes an increase in weld nugget size. Increasing the weld nugget size, increases the cross-tension load which can be expected.

Fig. 15 shows the fracture modes of the S1 (a), S3 (b), S4 (c) and S5 (d) welded joints after the cross-tension test. Failure modes can significantly affect the energy absorption capability and load carrying capacity of RSW joints. Nugget pull out fracture mode generally provides a high plastic deformation and energy absorption capability. According to Fig. 15, nugget pull out fracture modes were observed for whole welded joints in HAZ after cross-tension.

Nugget pull out indicates that the welded joint acquires a sufficient resistance for static forces. Interfacial fracture mode was observed on S1 welded joint after tensile-shear test. Whereas, nugget pull out fracture was observed after cross-tension test on S1 welded joint. This result indicates that such connections performs better resistance to cross-tension load.

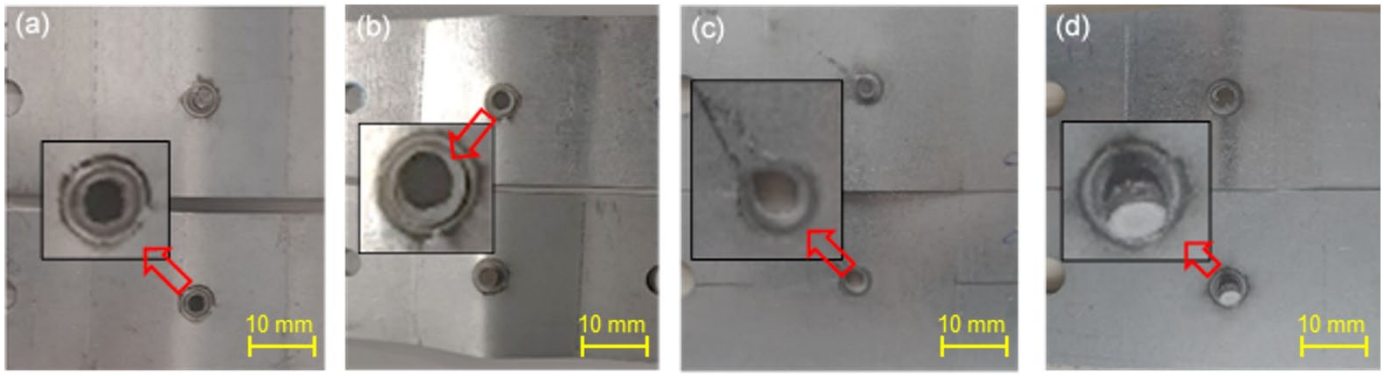

Fig. 15. The fracture modes of the S1 (a), S3 (b), S4 (c) and S5 (d) welded joints after the cross-tension test

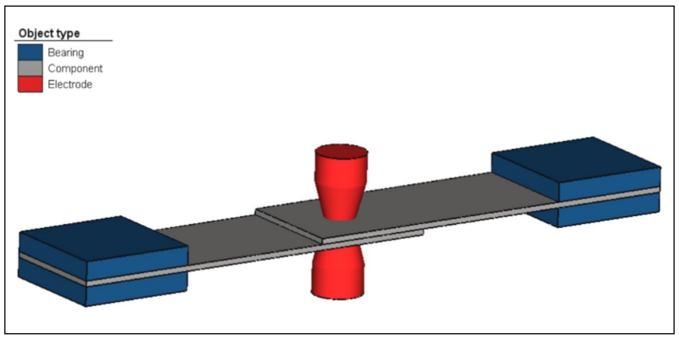

Fig. 16. The boundary conditions for performed simulation

3.5. Welding simulation results

Temperature gradients of 3 kA pre-pulse current were simulated in Simufact welding program.

Analysis boundary conditions visual is shown in Fig. 16. Chemical properties of materials, electromagnetic properties (electrical resistivity, conductivity), Thermal properties (melting point, solidus temperature and latent heat), TTT (Time-Temperature-Transformation) diagrams are entered as input to the FEA analysis program. Sheet metal specimens were fixed at both ends as seen in Fig. 16. In Fig. 17, the temperature values

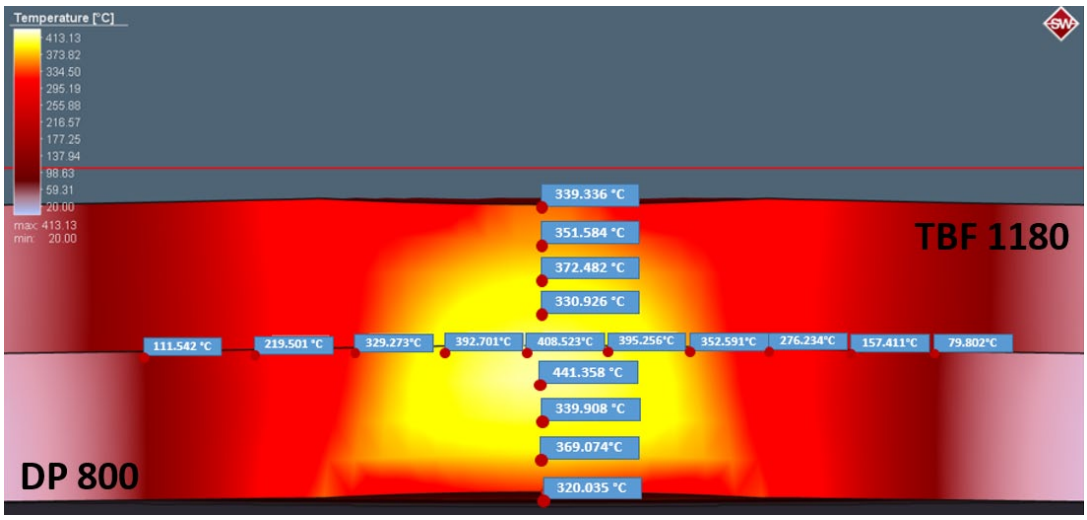

Fig. 17. Temperature values simulation results from the surface and interface of weld

occurred on the surface and centre were given. The highest temperature on the TBF1180 interface were obtained as 339°C and 441°C (Fig. 17), respectively. According to the results of the According to FEA (Finite Element Analysis) simulation, on surface of sheets pre-heating pulse was obtained below the melting temperature of Zn (~420°C). The pre-heating was applied to reduce the main pulse current heat input, avoid LME crack formation and improve welding quality.

3.6. Hardness test

Micro hardness measurements were carried out on the welded joints with different welding parameters in order to determine the hardness variation in the welding zone. Fig. 18 shows the typical micro hardness profiles with different welding currents including of three main weld zones on as base material, HAZ and weld metal. Variation was observed on the micro hardness values from base material to weld metal. In addition, diagonal hardness measurement points were also depicted as an image in Fig. 18.

The highest hardness values were obtained in HAZ. It was seen that HAZ has three different hardness values; 1 – the highest hardness of the coarse-grained zone nearby the weld metal, 2 – the soft zone nearby the base metal with a lower hardness than the base metal and 3 – the balanced transition zone between the highest and lowest hardness values.

Contrary to the Hall-Petch relation, the hardness increase in small grain-sized HAZ on both TBF 1180 and DP 800 region of the joint is lower than that of coarse grain-sized HAZ. However, it was occurred due to the differences in the cooling rates of the coarse-grained and fine-grained regions. In addition, the hardness increase/decrease in the region is not related to grain size, but to the tempering of hard phases such as martensite and bainite in the base metal in the welding thermal cycle.

In Fig. 18, it should be underlined that the hardness value decreased adjacent the both base metals. A tempered zone occurred during RSW located between the base metal and the HAZs

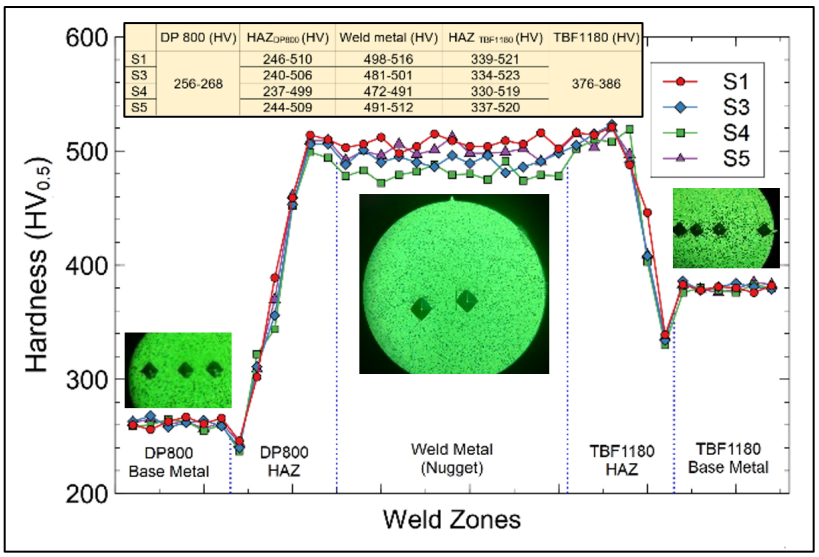

Fig. 18. Hardness measurement results

adjacent to nugget. This aforementioned zone is described as "Soft Zone" in the literature. Soft zone reduces the strength of the joint. Therefore, failure defects occur at the interface of the welded joint. Hardness value decreases due to the tempering of the martensite phases in HAZ during welding.

Several studies have been performed on the RSW of DP steels in the literature. It has been reported that the hard phases (eg. martensite) are tempered during RSW, resulting in a reduction in hardness in a narrow region adjacent to the base metal [35-38]. Besides, increased heat input play an important role on the reduction in hardness in this region. Pouranvari et all. [40] reported that longer cooling time also reduced the hardness value of this critical region on joining of AHSS by RSW.

In Fig. 18, highest hardness value was measured between 498-516 HV on S1 welded joint. The lowest hardness value was observed as 472-491 HV on the S4 welded joint. It was determined that increase in pre-pulse and main welding current slightly reduced the hardness of the weld metal due to the higher heat input and lower cooling rate during RSW. Yürük and Kahraman [39] reported that increased heat input (welding current and time) during RSW delayed cooling of the weld metal and thus the hardness of the weld metal decreased.

4. Conclusions

The effect of RSW MFDC technology on the microstructure and mechanical properties of GI coated DP800 and TBF1180 steels with different thicknesses were investigated. The test results are summarized as follows:

- LME formation can be avoided by MFDC technology with appropriate welding parameters on GI coated AHSS. According to macro structural investigation porosity, voids or incomplete gap could not be observed on the weld nugget and HAZ.
- The coarse-grained HAZ of the welded joints, which turned into fully austenite, generally transformed into bainitic and martensitic structures depending on the cooling rate after welding. In addition, while the both base metals have fine grain structure, a coarse grained structure was observed in the weld metal and HAZ adjacent to the melting border.
- Nugget sizes increased significantly with the increase of both pre-pulse and main welding currents by RSW. Therefore, the tensile-shear and cross-tension force carrying capacity of the welded joints increased. However, it was observed that the expulsion has a negative effect on the tensile-shear and cross-tension load carrying capacity.
- The highest strength values were obtained on S3 welded joint by tensile-shear and cross-tension tests as 17.60 kN and 5.51 kN, respectively. The failure mode type was realized in nugget pull-out failure mode (except S1 tensile-shear) after tensile-shear and cross-tension tests.
- As a result of the hardness measurements, similar hardness values were measured on the weld metal as well as adjacent close to the weld metal, but was observed higher than the base metals. In addition, a soft zone was found in the HAZ for both base metals. It was also concluded that higher heat input increased the proportion of softening in the HAZ. While the lowest hardness value of the DP800 soft zone region of the sample S1 was measured as 246 HV, this measurement was measured as 240 HV in the S2 coded sample and 237 HV in the sample S3. On the TBF 1180 side, the hardness test results were measured as 339 HV, 334 HV and 330 HV from sample S1 to S3, respectively.

Funding

This research did not receive any specific grant from National/International funding agencies.

REFERENCES

[1] Automotive Congress, Shengyang, China, October 30th, (2008).

[2] M. Hıdıroğlu, T.A. Başer, O. Tekelioğlu, N. Kahraman, Liquid metal embrittlement in resistance spot welding of third generation steels. 10th International Automotive Technologies Congress, 1546-1555 (2020).

[3] E. Tolf, Challenges in resistance welding of ultrahigh strength steels. First ed., Stockholm, Sweden, ISBN 978-91-7595-577-3 (2015).

[4] D. Bhattacharya, Liquid metal embrittlement during resistance spot welding of Zn-coated high strength steels. Mater. Sci. Technol. **34** (15), 1809-1809 (2018).
DOI: https://doi.org/10.1080/02670836.2018.1461595

[5] A.R. Marder, Metallurgy of zinc-coated steel. Progress in Materials Science **45**, 191-271 (2000).
DOI: https://doi.org/10.1016/S0079-6425(98) 00006-1

[6] D.R. Sigler, Observations of liquid metal-assisted cracking in resistance spot welds of zinc-coated advanced high strength steels. Sheet Met. Weld. Conf. XIII, Livonia, Mich., pp. 1-17 (2008).

[7] H. Gaul, S. Brauser, G. Weber, M. Rethmeier, Methods to obtain weld discontinuities in spot-welded joints made of advanced high-strength steels. Welding in the World **55**, 99-106 (2011).
DOI: https://doi.org/10.1007/BF03321547

[8] R. Ashiri, M.A. Haque, C.W. Ji, M. Shamanian, H.R. Salimijazi, Y.D. Park, Supercritical area and critical nugget diameter for liquid metal embrittlement of Zn-coated twining induced plasticity steels. Scripta Materialia **109** (1), 6-10 (2015).
DOI: https://doi.org/10.1016/j.scriptamat.2015.07.006

[9] D.Y. Choi, A. Sharma, S.H. Uhm, J.P. Jung, Liquid metal embrittlement of resistance spot welded 1180 TRIP steel: Effect of electrode force on cracking behavior. Metals and Materials International **25**, 219-228 (2018).
DOI: https://doi.org/10.1007/s12540-018-0180-x

[10] W. Jin, A. Lalachan, S.P. Murugan, C. Ji, Y. Park, Effect of Process Parameters and Nugget Growth Rate on Liquid Metal Embrittlement (LME) Cracking in the Resistance Spot Welding of Zinc-

Coated Steels. Journal of Welding and Joining **40** (6),464-467 (2022). DOI: https://doi.org/10.5781/JWJ.2022.40.6.2

[11] S.P. Murugan, V. Vijayan, C. Ji, Y.D. Park, Four types of LME cracks in RSW of Zn-coated AHSS. Welding Journal, 75-s, (2020). DOI: https://doi.org/10.29391/2020.99.008

[12] R. Sierlinger, M. Gruber, A cracking good story about liquid metal embrittlement during spot welding of advanced high strength steels. Voestalpine White Paper Stahl GmbH. https://www.voestalpine.com/division_stahl/content/download/52624/655464/file/VAST-W17008A%20White%20Paper%20Sierlinger.pdf

[13] T.A. Başer, Resistance Spot Welding of Zn-Coated Third Generation Automotive Steels Using Mid-Frequency Direct Current Technology. Trans. Indian. Inst. Met. **76**, 49-57 (2023). DOI: https://doi.org/10.1007/s12666-022-02771-7

[14] M. Kimchi, D.H. Phillips, Resistance spot welding: fundamentals and applications for the automotive ındustry. Synthesis Lectures on Mech. Eng. **1** (2), i-115 (2017). DOI: https://doi.org/10.2200/S00792ED1V01Y201707MEC005

[15] R. Ashiri, M. Shamanian, H.R. Salimijazi, M.A. Haque, J.H. Bae, C.W. Ji, K.G. Chin, Y.D. Park, Liquid metal embrittlement-free welds of zn-coated twinning ınduced plasticity steels. Scr. Mater. **114** (1), 41-47 (2016).

[16] Worldautosteel Liquid Metal Embrittlement Study. (2020). https://www.worldautosteel.org/projects/liquid-metal-embrittlement/

[17] E. Biro, Y. Zhou, Effect of multiple pulse resistance spot welding schedules on liquid metal embrittlement severity. Journal of Manufacturing Science and Engineering **141** (10), 1-9 (2019). DOI: https://doi.org/10.1115/1.4044099

[18] İ. Yilmaz, A.Y. Bilici, H. Aydin, Resistance spot weldability of TBF steel sheets with dissimilar thickness. Metall. Res. Technol. **117**, 620 (2020). DOI: https://doi.org/10.1051/metal/2020071

[19] M. Pouranvari, S.P.H. Marashi, Critical review of automotive steels spot welding: process, structure and properties. Sci. Technol. Weld. Join. **18** (5), 361-403 (2013).

[20] N.T. Williams, J.D. Parker, Review of resistance spot welding of steel sheets – part 1 modelling and control of weld nugget formation. Int. Mater. Rev. **49** (2), 45-75 (2004).

[21] Y. Luo, J. Liu, H. Xu, C. Xiong, L. Liu, Regression modeling and process analysis of resistance spot welding on galvanized steel sheet. Mater. Des. **30** (7), 2547-2555 (2009).

[22] J. Mendala, Liquid metal embrittlement of steel with galvanized coatings. IOP Conf. Ser. Mater. Sci. Eng. **35** (1) (2012).

[23] Y.G. Kim, I.J. Kim, J.S. Kim, Y. Il. Chung, D.Y. Choi, Evaluation of surface crack in resistance spot welds of Zn- Coated steel. Mater. Trans. **55**, 171 (2014).

[24] Z. Ling, T. Chen, L. Kong, M. Wang, H. Pan, M. Lel, Liquid Metal Embrittlement Cracking During Resistance Spot Welding of Galvanized Q&P980 Steel. Metall. Mater. Trans. A **50**, 5128-5142 (2019). DOI: https://doi.org/10.1007/s11661-019-05388-6

[25] H. Aydın, İ. Yılmaz, A.Y. Bilici, Investigation of microstructure and mechanical properties of dissimilar electrical resistance spot welded TBF/DP600 steel sheets. Journal of the Faculty of Engineering and Architecture of Gazi University **37**, 2 609-624 (2022).

[26] M. Stadler, M. Gruber, R. Schnitzer, C. Hofer, Microstructural characterization of a double pulse resistance spot welded 1200 MPa TBF steel. Welding in the World, Le Soudage Dans Le Monde **64** (4), (2019). DOI: https://doi.org/10.1007/s40194-019-00835-9

[27] S.S.G. Banadkouki, E. Fereiduni, Effect of prior austenite carbon partitioning on martensite hardening variation in a low alloy ferrite–martensite dual phase steel. Mater. Sci. Eng. A. **619**, 129-136 (2014).

[28] X.Q. Zhang, G.L. Chen, Y.S. Zhang, Characteristics of electrode wear in resistance spot welding dual-phase steels. Materials & Design **29**, 1, 279-283 (2008).

[29] Y. Kaya, N. Kahraman, The effects of electrode force, welding current and welding time on the resistance spot weldability of pure titanium. The International Journal of Advanced Manufacturing Technology **60** (1-4), 127-134 (2012).

[30] S. Fukumoto, K. Fujiwara, S. Toji, A. Yamamoto, Small-scale resistance spot welding of austenitic stainless steels. Materials Science and Engineering A **492** (1-2), 243-249 (2008).

[31] D.Q. Sun, B. Lang, D.X. Sun, J.B. Li, Microstructures and mechanical properties of resistance spot welded magnesium alloy joints**,** Materials Science and Engineering A **460-461**, 494-498 (2007).

[32] P. Marashi, M. Pouranvari, S. Amirabdollahian, A. Abedi, M. Goodarzi, Microstructure and failure behavior of dissimilar resistance spot welds between low carbon galvanized and austenitic stainless steels. Materials Science and Engineering A **480** (1-2), 175-180 (2008).

[33] M. Pouranvari, E. Ranjbarnoodeh, DP600 / AISI1008 dissimilar resistance spot welding: on the reduction of energy absorption at high heat input welding condition Research Journal of Applied Sciences, Engineering and Technology, 1-4, (2012).

[34] P.R. Spena, M.D. Maddis, F. Lombardi Mechanical strength and fracture of resistance spot welded advanced high strength steels. Procedia Engineering **109**, 450-456 (2015). DOI: https://doi.org/10.1016/j.proeng.2015.06.262

[35] V.H.B. Hernandez, S.K. Panda, Y. Okita, N.Y. Zhou, A study on heat affected zone softening in resistance spot welded dual phase steel by nanoindentation. Journal of Materials Science **45** (6), 1638-1647 (2010).

[36] V.H.B. Hernandez, M.L. Kuntz, M.I. Khan, Y. Zhou, Influence of microstructure and weld size on the mechanical behaviour of dissimilar AHSS resistance spot welds. Science and Technology of Welding and Joining **13** (8), 769-776 (2008).

[37] X. Sun, E.V. Stephens, M.A. Khaleel, Effects of fusion zone size and failure mode on peak load and energy absorption of advanced high-strength steel spot welds. Welding Journal **86** (1), 18-25 (2007).

[38] M. Pouranvari, S.P.H. Marashi, D.S. Safanama, Failure mode transition in AHSS resistance spot welds. Part II: experimental investigation and model validation. Materials Science and Engineering A **528** (29-30), 8344-8352 (2011).

[39] A. Yürük, N. Kahraman, Weld zone characterization of stainless steel joined through electric resistance spot welding. Int. J. Adv. Manuf. Technol. **92**, 2975-2986 (2017).